

Dynamic changes in network synchrony reveal resting-state functional networks

Vesna Vuksanović^{1,2, a)} and Philipp Hövel^{1,2}

¹⁾*Institut für Theoretische Physik, Technische Universität Berlin, Hardenbergstraße 36, 10623 Berlin, Germany*

²⁾*Bernstein Center for Computational Neuroscience, Humboldt-Universität zu Berlin, Philippstraße 13, 10115 Berlin, Germany*

(Dated: 18 September 2021)

Experimental fMRI studies have shown that spontaneous brain activity i.e. in the absence of any external input, exhibit complex spatial and temporal patterns of co-activity between segregated brain regions. These so-called large-scale resting-state functional connectivity networks represent dynamically organized neural assemblies interacting with each other in a complex way. It has been suggested that looking at the dynamical properties of complex patterns of brain functional co-activity may reveal neural mechanisms underlying the dynamic changes in functional interactions. Here, we examine how global network dynamics is shaped by different network configurations, derived from realistic brain functional interactions. We focus on two main dynamics measures: synchrony and variations in synchrony. Neural activity and the inferred hemodynamic response of the network nodes are simulated using system of 90 FitzHugh-Nagumo neural models subject to system noise and time-delayed interactions. These models are embedded into the topology of the complex brain functional interactions, whose architecture is additionally reduced to its main structural pathways. In the simulated functional networks, patterns of correlated regional activity clearly arise from dynamical properties that maximize synchrony and variations in synchrony. Our results on the fast changes of the level of the network synchrony also show how flexible changes in the large-scale network dynamics could be.

Keywords: network dynamics; whole brain simulations; FitzHugh-Nagumo neural model

Experimental studies of the human brain activity at rest i.e. without any overt-directed behavior have revealed patterns of correlated activity, so called resting-state networks. The neural mechanisms contributing to the formation of these networks are largely unknown. We use modeling approach to interpret these experimental findings, looking at the brain as the dynamical system. We characterize brain network dynamical properties by synchrony and variability in synchrony. We demonstrate that functional brain interactions may arise from the network dynamics which allow flexible changes between different network configurations. We show that these changes reflect almost periodic alternations between network synchronized and desynchronized state.

The mechanisms generating these patterns of correlated activity, also called resting-state functional networks are largely unknown. It has been suggested that they reflect a complex interplay between brain structural connections and the dynamics of interacting neuronal units^{5,12}. Theoretical models of the large-scale brain resting-state activity have explored the range of conditions that might govern intrinsic brain processes and contribute to the generation of correlated fluctuations between segregated brain areas^{9,21,22}. Particular attention has been paid to the properties of the network dynamics that enable the emergence of a metastable state, which represents the network's tendency to switch between synchronized and desynchronized states and thus, explore different network configurations^{9,13,18,32}. One approach to observe metastable network states in brain dynamics is to consider self-sustained oscillatory local neural dynamics and neural signal transmission delays in the interactions between network elements^{8,9,13}. Similarly, the coupling strength and signal transmission delays in the interactions between noise-driven neural oscillators, enable generation of the spatio-temporal correlated low-frequency (< 0.1 Hz) fluctuations in the dynamics of the resting brain^{18,19}.

Other important ingredients of the large-scale brain dynamics models are complex brain network interactions expressed usually in the form of the connectivity matrix. The matrix elements represent the anatomical connection strengths inferred from all possible structural connections between anatomically defined regions of interest (ROIs). Using this approach, the large-scale network dy-

I. INTRODUCTION

Well organized spatio-temporal low-frequency fluctuations (< 0.1 Hz) have been observed in blood-oxygen-level-dependent (BOLD) functional magnetic resonance imaging (fMRI) signals of a mammalian brain in the absence of any stimulation or task-related behavior^{2,10,40}.

^{a)}Electronic mail: vesna.vuksanovic@bccn-berlin.de

namics models are built on matrices of the human^{8,9,22} or monkey^{13,19,21} brain architectures. Both empirical and numerical findings suggest that the brain structural and functional architectures (or networks) share many common features⁵. However, in contrast to structural networks, the functional networks of the brain undergo permanent reconfiguration of their connections depending on brain cognitive state^{1,20}. Moreover, altered topology of brain networks is indicator of pathological state⁷.

We combine these approaches to investigate properties of the network dynamics that underlie patterns of spatio-temporal correlations of resting-state functional networks. In addition, we consider the contribution of the long-distance functional interactions i.e. those that are not supported by direct neural paths between the interacting brain areas. In our previous work⁴¹, we have shown that the long-distance functional correlations may emerge from relay-like interactions between neural oscillators that share large parts of their individual network neighborhoods. Here, we aim to explore, if these types of the spatio-temporal relations may also emerge in the network dynamics subject to system noise and signal propagation delays. For this purpose, we chose to model the local node dynamics by noise-driven excitable FitzHugh-Nagumo (FHN) neurons oscillating at 15 Hz. Our approach is similar to those of Ghosh and colleagues¹⁹, however, different in the two main model ingredients: (i) we use a connectivity matrix derived from diffusion weighted brain imaging data, and (ii) we take into account functionally realistic network interactions that are also supported by physical (structural) connections. Additionally, in our analysis of the simulated dynamics, we focus on network metastability rather than linear approximation of its stability.

Through simulations of computational models of resting-state functional correlations, we show that the neural network dynamics display fast transitions between synchronized and desynchronized states. These transitions give rise to spatio-temporal correlation patterns that resemble to those found in resting-state fMRI experiments.

II. METHODS

A. Extraction of network topology

To build a model of the neural network dynamics on functionally realistic network interactions, we have combined empirically derived structural and resting-state functional maps similarly to our previous study⁴¹. In short, these maps were extracted from the 90 brain regions parcellated according to the Tzourio-Mazoyer brain atlas³⁸ using the automated anatomical labeling (AAL) method. The full list of regions considered in the analysis is given in the Table I.

The structural connectivity is estimated from diffusion weighted brain imaging data, according to the procedure

described in²³. The procedure maps out probabilities for the presence of the direct neural connections between any pairs of the 90 considered anatomical ROIs. We will therefore refer to this map as to the anatomical connection probability (ACP) map or matrix²³. The functional connectivity (FC) matrix is extracted from BOLD fMRI data of 26 subjects^{25,41}. The matrix entries represent pairwise temporal correlation coefficients between ROIs mean BOLD time series estimated from the total scanning time (7.5 minutes).

To derive the coupling topology for the network model used in the simulations, we combined structural and functional connectivity matrices in the following way. Given the statistical nature of FC and ACP entries we first applied a binarization method to extract only statistically significant connections. By doing that we also took into account the conditions that allow comparisons between brain structural and functional networks³⁹. Binarization is done by applying thresholds r and p for the FC and ACP matrix, respectively. If matrix values are greater than or equal to the threshold values, then the corresponding element of the adjacency matrix is set to 1; otherwise it is set to 0. For the FC matrix, we have used thresholds in the interval $r = [0.52, 0.53, \dots, 0.65]$, and for the ACP matrix only one value $p = 0.05$ (see Fig. 1). The lowest value for r and the value for p are chosen such that both networks have equal connection density $\kappa = 0.5$ ³⁹. The upper boundary for r is the highest threshold at which the FC network still comprises one component. We then use the element-wise product of these binarized matrices as a coupling topology for the simulations. As a result, we preserve those strongly pronounced interactions of the functional networks that are connected via direct anatomical links, that is, regions without direct anatomical links are not directly coupled in the simulations. This procedure is previously described in detail in⁴¹. For an exemplary visualization of the resulting brain network see Fig. 2.

B. Simulation of network dynamics - neural and BOLD activity

To infer the BOLD signal in dependence on the network properties, we first simulate the underlying neural activity. We consider the neural dynamics on the network of $N = 90$ cortical regions whose local dynamics are represented by the homogeneous FitzHugh-Nagumo (FHN) neurons.

1. Network of FitzHugh-Nagumo neural models

We model neural network dynamics by embedding individual FHN neural model into each of the 90 cortical regions, according to the connectivity matrix $\{a_{ij}\}$, $i, j = 1, \dots, N$. FHN neural model can be described by two state variables u and v , representing activator (membrane

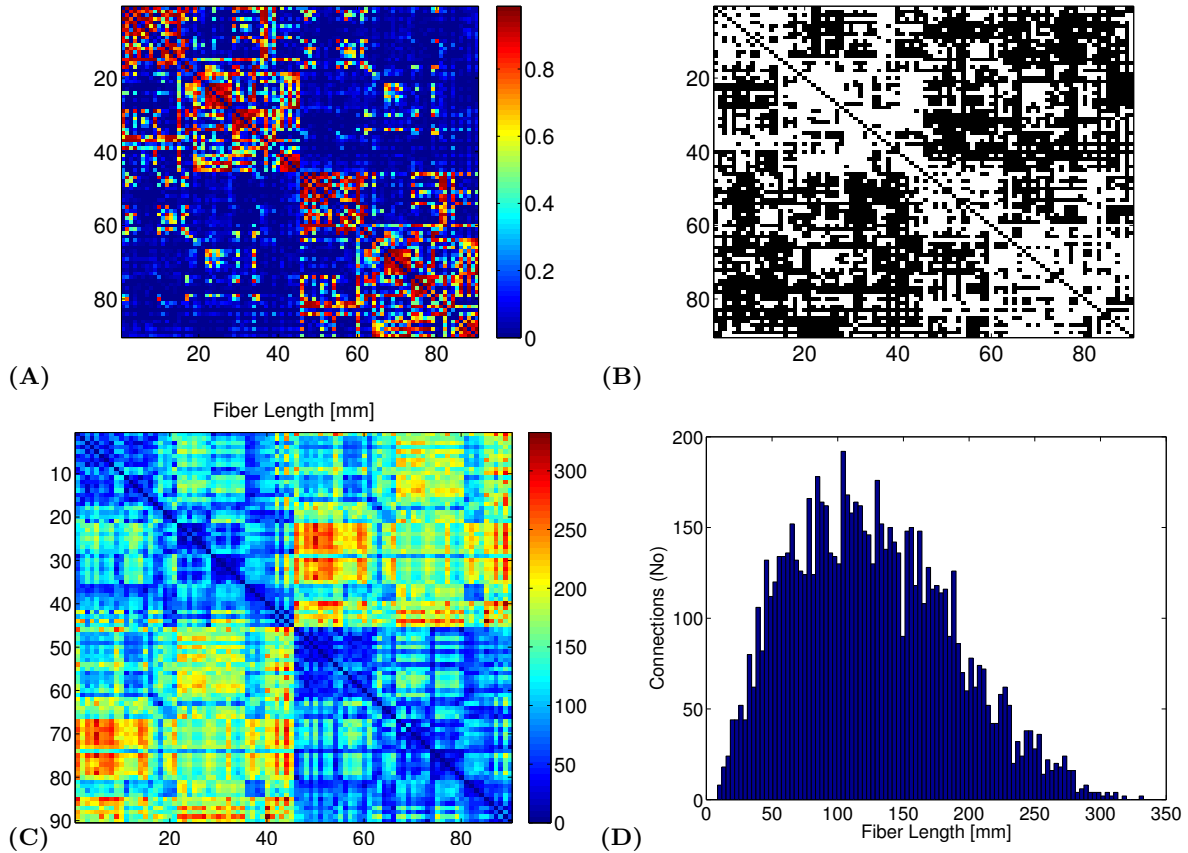


FIG. 1. **Functionally realistic connectivity between 90 brain regions considered in the model.** (A) Anatomical connectivity probability (ACP) matrix and (B) its binarized version when the threshold $p = 0.05$ is applied. Application of the threshold to the ACP matrix enables also that the homologous interactions, which are usually not good resolved by DW-DTI analysis method, are represented with the equal probabilities in the model. (C) The fiber lengths between the pairs of nodes and (D) corresponding number of the connections. The matrices are ordered according to the regions listed in Table I. First 45 regions belong to the right hemisphere.

potential) and inhibitor (recovery variable), according to the following dynamical equations:

$$\dot{u} = g(u, v) = \tau \left(v + \gamma u - \frac{u^3}{3} \right) \quad (1a)$$

$$\dot{v} = h(u, v) = -\frac{1}{\tau} (u - \alpha + \beta v - I), \quad (1b)$$

where I is magnitude of an external stimulus, which is assumed to be 0^{19} . In order to obtain the dynamics of an isolated node in a damped oscillatory regime [as shown in Fig. 3 (A – upper panel)], we consider the following system parameters throughout this paper: $\alpha = 0.85$, $\beta = 0.2$, $\gamma = 1.0$, and $\tau = 1.25$.

To combine FHN units in a network, we utilize the following equations¹⁹:

$$\dot{u}_i = g(u_i, v_i) - c \sum_{j=1}^N a_{ij} u_j(t - \Delta t_{ij}) + n_u \quad (2a)$$

$$\dot{v}_i = h(u_i, v_i) + n_v, \quad (2b)$$

where u_i and v_i are the activator and inhibitor variables, located at node i . c denotes a global coupling parameter ($c > 0$) and a_{ij} are the elements of the connectivity matrix, defined above. Δt_{ij} denote time delays. n_u and n_v are two independent additive white Gaussian noise terms with zero mean, unity variance and noise strength D . The influence of the applied noise level on dynamics of an isolated node is shown in the Fig. 3 (A – lower panel). When coupled in the network, the dynamical behavior of a node changes to the oscillatory regime. The frequency distribution of the noise-driven oscillations of a node is centered around 15 Hz as shown in Fig. 3(B).

We solve the system of coupled differential equations with time delays and additive noise using the PYTHON-module PYDELAY¹⁵. The algorithm is based on the Bogacki-Shampine method^{3,35}, which is also implemented in MATLAB'S DDE23 routine. We calculate time delays for a physiologically realistic value of the signal propagation velocity v via $\Delta t_{ij} = d_{ij}/v$, where d_{ij} are given by the lengths of the actual three-dimensional tra-

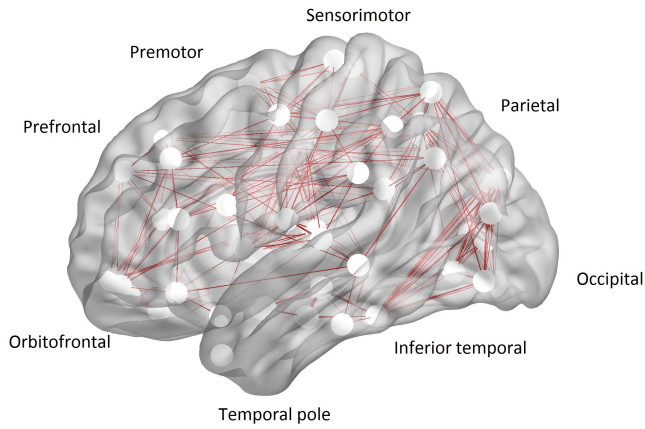


FIG. 2. **Visualization of brain functional networks.** The position of the network nodes is given according to the coordinates of the centre of the mass of the AAL cortical regions in MNI space. Size of the node is proportional to its degree for threshold $r = 0.57$. List of regions is given in Table I.

jectory of the fiber tract between centers of the regions, i.e. network nodes i and j . A color-coded representation of the d_{ij} values is shown in Fig. 1(C). We use a single value for the signal propagation velocity $v = 7$ m/s throughout the study.

We simulated 450s of the real-time neural activity sampled at a time step of 0.001 s for a range of the coupling strengths c and thresholds r . When time delays, system noise and global coupling term are taken into account, the simulated dynamics of the neural activity exhibits a behavior exemplary shown in Fig. 4.

2. Measures of the network dynamics

To quantify global network dynamics we define two different measures: the synchrony of the neural activity and metastability, which is defined by fluctuations in synchrony over time. Here, we have followed a general framework to study synchronization phenomena in a network of coupled oscillators, given by Kuramoto and colleagues^{24,37}. To apply this framework on the FHN system we first need to define phase-like variables θ_i . This can be done using one of the several approaches valid for the FHN models^{27,29}. However, due to the presence of the noise term in our model, we have chosen to use the Hilbert transform. The transform gives a time series of complex numbers with a real and an imaginary part, which then can be used to calculate instantaneous phases θ_i for the each node as the argument of this complex number³¹.

The synchrony of the simulated network dynamics is evaluated across all oscillators in the network, using the

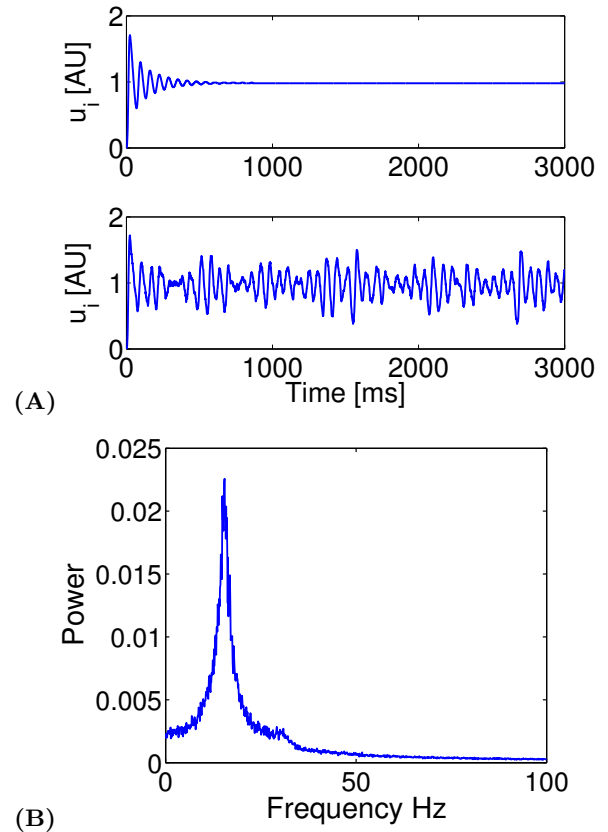


FIG. 3. **Time evolution of the activator u_i variable of the FitzHugh-Nagumo neural model for an isolated node.** (A) Top panel represents node dynamics without noise and bottom panel shows dynamics of the same node when noise is added via the term n_u , as described in the Eq. 2. (B) Fourier spectrum of the neural activity of an isolated node under the system noise. The peak frequency is at around 15 Hz. System parameters: $\alpha = 0.85$, $\beta = 0.2$, $\gamma = 1.0$, $\tau = 1.25$, and $p = 0.05$.

order parameter $R(t)$ ³⁷:

$$R(t) = \left| \left\langle e^{i\theta_j(t)} \right\rangle \right|, \quad j = 1, \dots, N, \quad (3)$$

where $\langle \cdot \rangle$ denotes average over all nodes in the network. The order parameter measures the cooperative dynamics in the network and can have any value between 0 and 1²⁸. The closer $R(t)$ to unity, the higher the level of global synchrony in the network. The network is in a desynchronized state for $R(t) = 0$.

In neural networks, however, $R(t)$ is never equal to 1 nor 0, i.e. neural networks never reach a fully synchronized nor desynchronized state. Instead, the brain network dynamics exhibits large variability, and the amount of global synchrony of network nodes vary over time, indicating transitions from a synchronized to more desynchronized state^{11,14}. This metastable state in brain dynamics can be quantified by the standard deviation σ_R of the order parameter $R(t)$ ^{9,36}. It has been suggested

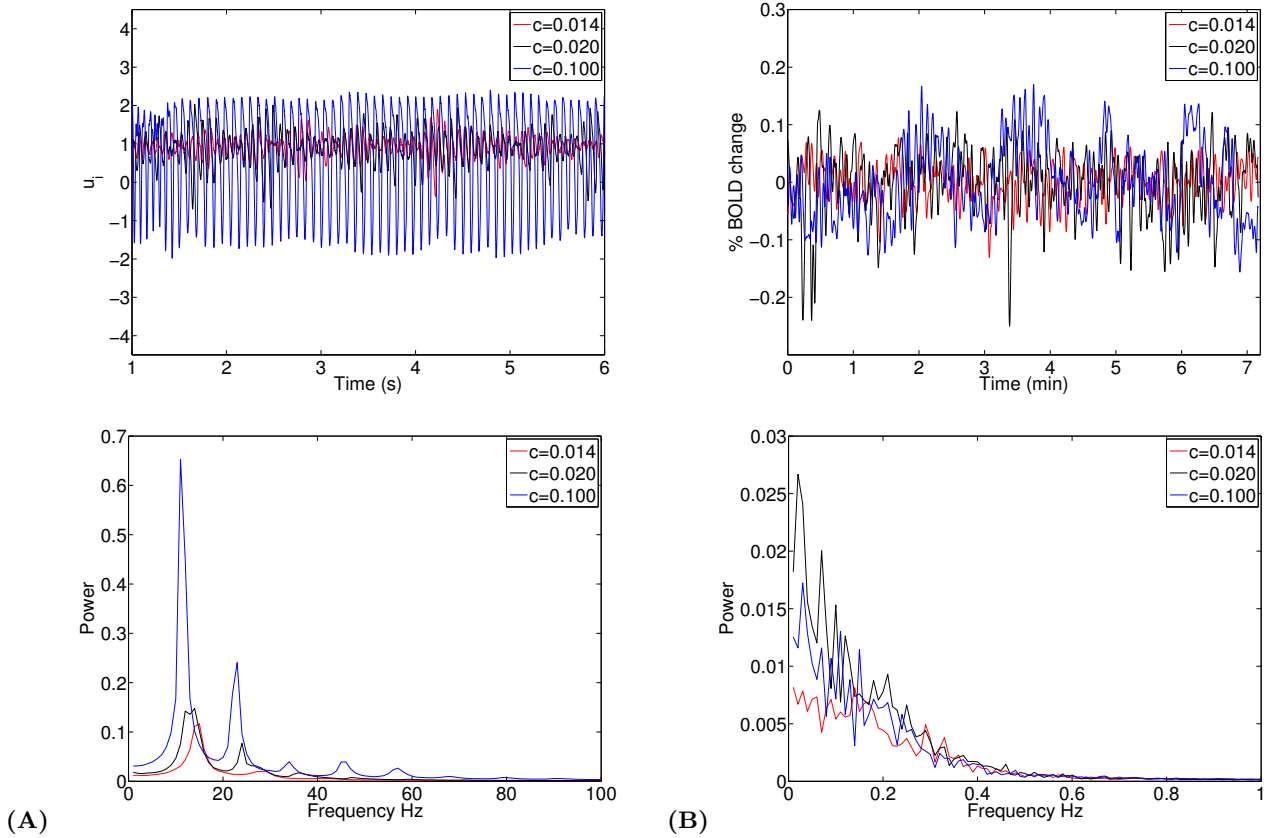


FIG. 4. **Time series and the corresponding Fourier power spectra of (A) neural and (B) BOLD activity** of the representative network node ($i = 28$) for three different coupling strengths c and a fixed threshold $r = 0.57$. The node has 20 nearest neighbors for this particular threshold, which corresponds to the average number of the links in the network. System parameters as in Fig. 3.

that the brain network dynamics operate in a state that maximizes synchrony and metastability^{20,36}.

3. Modeling BOLD activity and functional networks

Low-frequency (< 0.1 Hz) oscillatory dynamics of BOLD signal is inferred from the simulated neural activity using the Balloon-Windkessel model¹⁷. The model describes the relationship between changes in the regional blood flow, caused by local neural activity, and the BOLD signal, which is presented as a function of venous volume and deoxyhemoglobin content. We implemented the model using default parameters values provided within SPM8¹⁶.

An important component of the BOLD model is a neural signal as a main input. It can be given in the form of either neural spiking rate or local field potential³⁴. To calculate BOLD activity, we feed the time series of the activator variables u_i , which resemble membrane potentials, into the model. Representative time series of modelled BOLD activity and corresponding power spectra are

shown in Fig. 4(B) for different coupling strengths.

In order to quantify the functional connectivity between nodes i and j from the simulated BOLD activity, we calculate pairwise Pearson correlation coefficient:

$$\rho(i, j) = \frac{\langle V_i(t)V_j(t) \rangle - \langle V_i(t) \rangle \langle V_j(t) \rangle}{\sigma(V_i(t))\sigma(V_j(t))}, \quad (4)$$

where $V_i(t)$ represents the time series of the activity of the node i at time t , σ is its standard deviation, and $\langle \cdot \rangle$ denotes temporal averages.

4. Complex network measures of simulated functional networks

In our simulations, we use the network interactions – derived from experimental fMRI and DW-DTI data – as coupling topologies. They can be characterized using graph-theoretical measures across range of correlation thresholds. In the Fig. 9 we show some measures derived from the coupling topology at the matrix threshold $r = 0.57$. The following network properties are calculated as defined in Ref.³³:

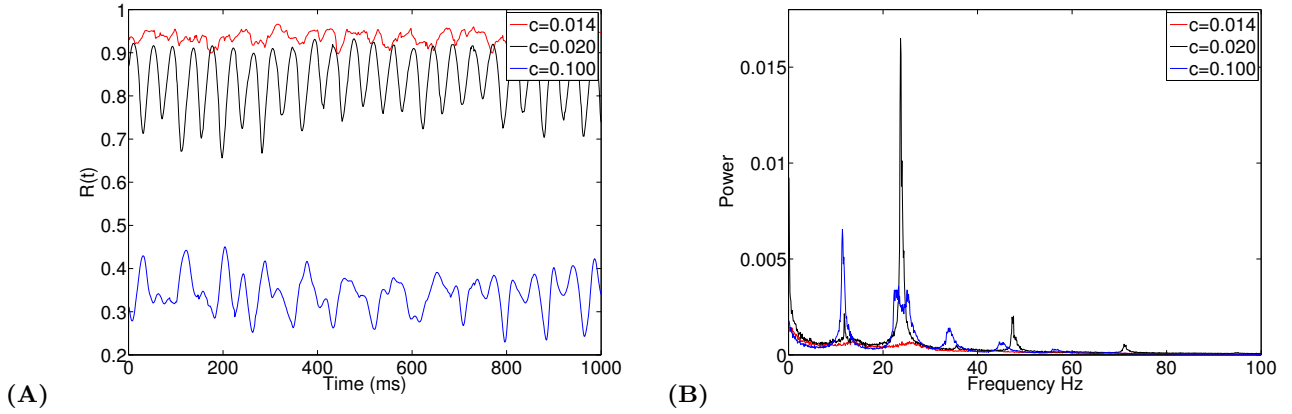


FIG. 5. **Global synchrony** as a function of (A) time and (B) frequency, for three different coupling strengths c as indicated in the legend, and the network topology at the threshold $r = 0.57$. System parameters as in Fig. 3.

Degree: The number of connections with the other nodes in the network. Degree of a node i is calculated

$$k_i = \sum_{j=1}^N a_{ij}, \quad (5)$$

where, a_{ij} represents connection between nodes i and j : $a_{ij} = 1$ if there is a connection between nodes and $a_{ij} = 0$ otherwise.

Clustering coefficient: Ratio of the number of connections in the neighborhood of a node and the number of connections if the neighborhood was fully connected. Clustering coefficient of the network is calculated as

$$C = \frac{1}{N} \sum_{i=1}^N C_i = \frac{1}{N} \sum_{i=1}^N \frac{2t_i}{k_i(k_i - 1)}, \quad (6)$$

where C_i is the clustering coefficient of node i and t_i is number of triangles around a node i .

Global efficiency: The average inverse shortest path length between the node and its neighbors. Global efficiency of the network is calculated as

$$E = \frac{1}{N} \sum_{i=1}^N E_i = \frac{1}{N} \sum_{i=1}^N \frac{\sum_{j=1, j \neq i}^N d_{ij}^{-1}}{N-1}, \quad (7)$$

where the shortest path length d_{ij} between nodes i and j is defined by the number of links between the respective nodes, that is,

$$d_{ij} = \sum_{a_{uv} \in g_{i \leftrightarrow j}} a_{uv}, \quad (8)$$

where $g_{i \leftrightarrow j}$ is the shortest path between i and j . Note that $d_{ij} = \infty$ for all unconnected pairs i, j .

Characteristic path of the network:

$$L = \frac{1}{N} \sum_{i=1}^N L_i = \frac{1}{N} \sum_{i=1}^N \frac{\sum_{j=1, j \neq i}^N d_{ij}}{N-1}, \quad (9)$$

where d_{ij} is the shortest path length (distance) between nodes i and j defined above.

III. RESULTS

In our simulations we consider functionally realistic network interactions, i.e. those that take into account structurally supported connectivity between functionally related network nodes, and chose to model each node's dynamics by a simple FHN neuronal model. The node dynamics is tuned such that each isolated node displays damped oscillations (see Fig. 3(A) upper panel). However, noise added to the system drives each FHN element from its equilibrium to an oscillatory state. The frequency of the oscillations of an isolated node with the added noise is around 15 Hz (as shown in Fig. 3). We aim to explore how the global network dynamics is influenced by the underlying topology and the strengths of the interactions. Therefore, focusing on the role of the network interactions in the collective behavior, we kept neural signal transmission velocity at the constant value ($v = 7$ m/s). This represents a biologically realistic value for the neural signal propagation and also an optimal value to obtain desired brain network dynamics in the system of the FHN elements¹⁹.

In order to investigate complex collective network dynamics we study the global level of the network synchrony and its variation, i.e. metastability as a function of the global coupling strength and coupling topology. We simulated 7.5 min of the whole network dynamics to match experimental fMRI time series. Figure 6 shows how the level of network synchrony, calculated by time-averaged order parameter $\langle R(t) \rangle$ given in Eq. 3, varies depending on the free model parameters c and r . We see in Fig. 6(A) that the global level of synchrony ranges from fully synchronized ($\langle R \rangle = 1$) to desynchronized ($\langle R \rangle = 0$) states, depending on the choice of r and c . The resting-brain dynamics hardly show either extreme. Instead, they are

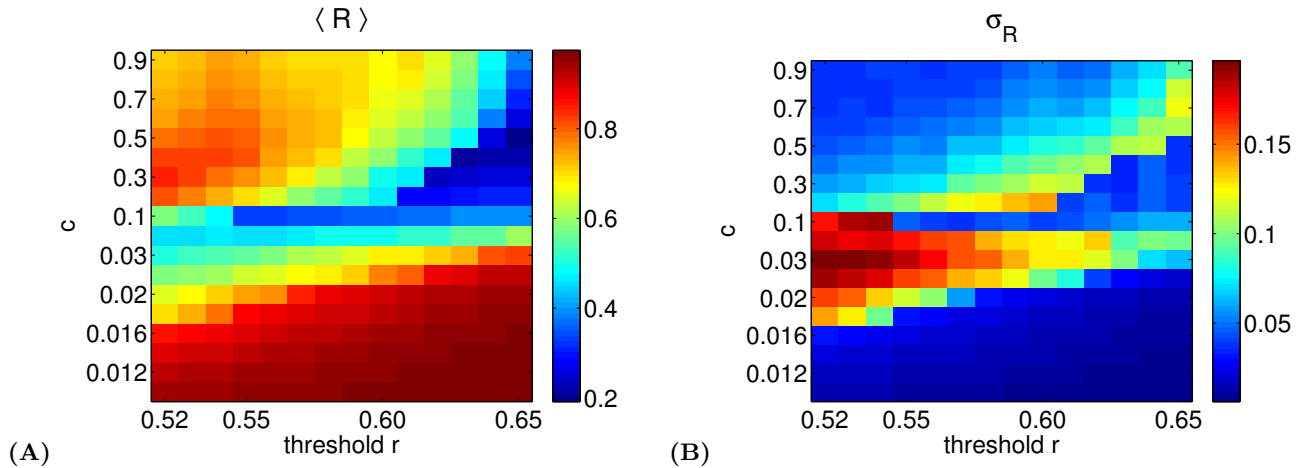


FIG. 6. **Global measures of the network dynamics.** (A) Mean order parameter $\langle R(t) \rangle$ and (B) metastability, i.e. variations in synchrony σ_R in the parameter space of the global coupling strength c and the correlation threshold r . System parameters as in Fig. 3.

characterized by metastable states. Hence, we calculate the standard deviation of the global order parameter as an indicator of this metastability, as shown in Fig. 6(B). For small c and over all examined network configurations (all examined thresholds r), as well as for large c and higher values of the network density (low r), the networks show high synchronization indicated by red areas in Fig. 6(A). This regime, however, corresponds to robust full synchronization, which does not allow large variability. Accordingly, $R(t)$ does not show pronounced fluctuations. However, as shown in Fig. 6(B), variations in synchrony display considerable level only for the narrow range of c and r , as indicated by red color. In this area of the parameter space, simulated network dynamics undergo permanent changes from synchronized to a less synchronized state. At the same time, this area corresponds to the region where the agreement between the simulations and the experiment is the best (as shown in Fig. 7). It can be seen that the simulations and the experiment show best agreement within the region in the parameter space where the network shows considerable amount of synchrony ($\langle R \rangle \approx 0.5$) and metastability ($\sigma_R \approx 0.15$). Thus, we consider these values as the most relevant regions of the network synchrony and metastability.

To quantify the dynamic network's variations in synchrony, we calculated fast Fourier transform of time-averaged order parameter $R(t)$. As shown in Fig. 5(A), as the coupling strength between the nodes increases, the order parameter starts to fluctuate in more periodic manner, indicating almost periodic network's transitions between synchrony and asynchrony. The frequency of these transitions settles around 10 Hz, for $c \geq 0.02$. See Fig. 5(B).

To study the network properties that contribute to the dynamic behavior in the most relevant region, we have performed graph theoretical analysis on the empirical network used as the coupling topology in the one of

the simulation ($r = 0.57$). We have chosen this particular network configuration since the simulated dynamics based on this topology show the best agreement with the experiment (see Fig. 7). In Fig. 9, we show node-wise network properties: degree, clustering coefficient and global efficiency. Clustering coefficient (CC) is used to identify hubs in the network. CC values as high as 0.5 together with large degrees indicate that a node qualifies as hub²⁶. Considering the nature of the interactions in the coupling topology we calculate the global node efficiency (GE), which represents “a measure of the overall capacity for parallel information transfer and integrated processing”⁶. We see that at this correlation threshold significant number of nodes show relatively high GE values. It has been already suggested that this network property play role in the metastable state in neural synchrony³⁶.

IV. DISCUSSION

In this work we have examined role of network configurations and synchronization dynamics in the emergence of resting-state functional correlations. Using numerical simulations of the neural network dynamics, based on the FHN neural models embedded into functionally realistic network structure and subject to noisy time-delayed interactions, we have investigated the network dynamics' transitions from synchronized to desynchronized state. We have found that the best agreement between the model and the experiment lie in the region where network dynamics maximizes synchrony and variations in synchrony.

To understand how functional correlations between segregated brain areas arise from underlying functional interactions, supported by the actual neural link between them, we use computational simulations and hu-

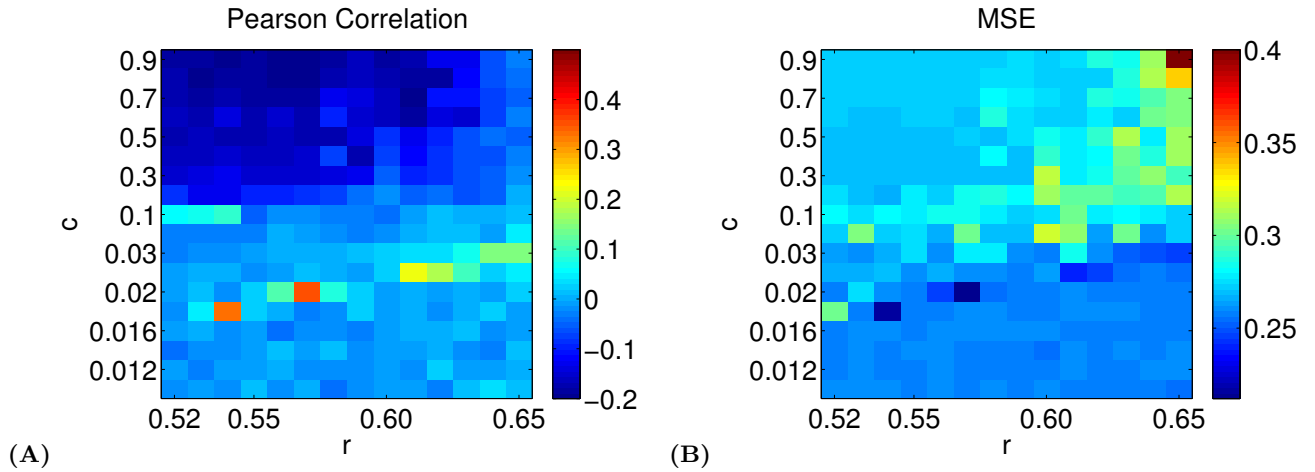


FIG. 7. **Pearson correlation coefficient** between experimental and simulated functional connectivity (A) and means squared error (B) in the parameter space of the global coupling strength c and the correlation threshold r . System parameters as in Fig. 3.

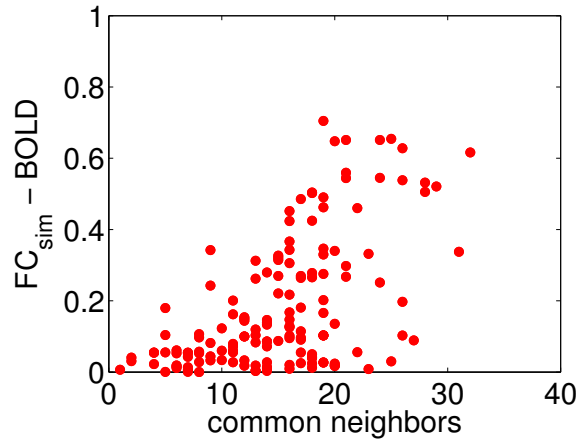


FIG. 8. **Functional connectivity (FC) between pairs of network nodes as a function of nearest neighbors.** Only nodes coupled via indirect connections are represented. Data are shown for FC network simulated on the network topology at the threshold $r = 0.57$ and for the coupling strength $c = 0.02$ (Pearson correlation $\rho = 0.51$ $p < 0.01$).

man brain imaging data. First, we have extracted the network topology for our model using empirically obtained brain structural and functional connectivities (see Fig. 1). This takes into account changes in the network interactions similar to those observed experimentally. We explore conditions that allow the dynamical properties of the brain networks – synchrony and variations in synchrony – to arise from different network configurations generating patterns of correlated activity between the brain regions. By varying the network topologies in a range of experimentally realistic values^{5,39} and tuning the global coupling strength, we obtained the correla-

tions patterns in the simulated BOLD time series very similar to those found in the experiment. We show that flexible changes in the network dynamics – fast periodic changes in the global level of synchrony (see Fig. 5) – produce functionally possible network dynamics. This shows how flexible changes in the large-scale networks dynamics could be. However, we also show that this is the case only if both dynamical properties of the network – synchrony and variations in synchrony – are maximized (as indicated by green/yellow and red colors in Fig. 6(A) and (B), respectively).

It is worth noting that in agreement with our previous study⁴¹, here we also observed a similar dependence of the functional correlations between indirectly coupled network nodes on the number of their overlapping neighbors (as shown in Fig. 8). This important finding indicates that the result is robust with respect to the generation of the network dynamics. As for Kuramoto-like phase oscillators, oscillating in γ frequency range⁴¹, noise-driven FHN models, oscillating at around 15 Hz (i.e. in α band), display similar dynamic behavior. The correlation patterns of low-frequency BOLD activity, revealing FC networks, highly agree between the studies (see Fig. 5 in⁴¹) and also with the experiment. Moreover, these results are consistent with some previous findings showing that resting-state FC networks arise from different types of local dynamics^{4,9,13,21} and network topologies^{13,21}. We also would like to point out a single value for the propagation velocity ($v = 7$ m/s) used in our study. As some numerical studies have already shown, the system of the FHN neurons displays high sensitivity to the presence of the time delays in the coupling term^{29,30}. However, here we have not observed such a high sensitivity for the biophysiologicaly valid velocity values (between 5 and 20 m/s)¹⁹.

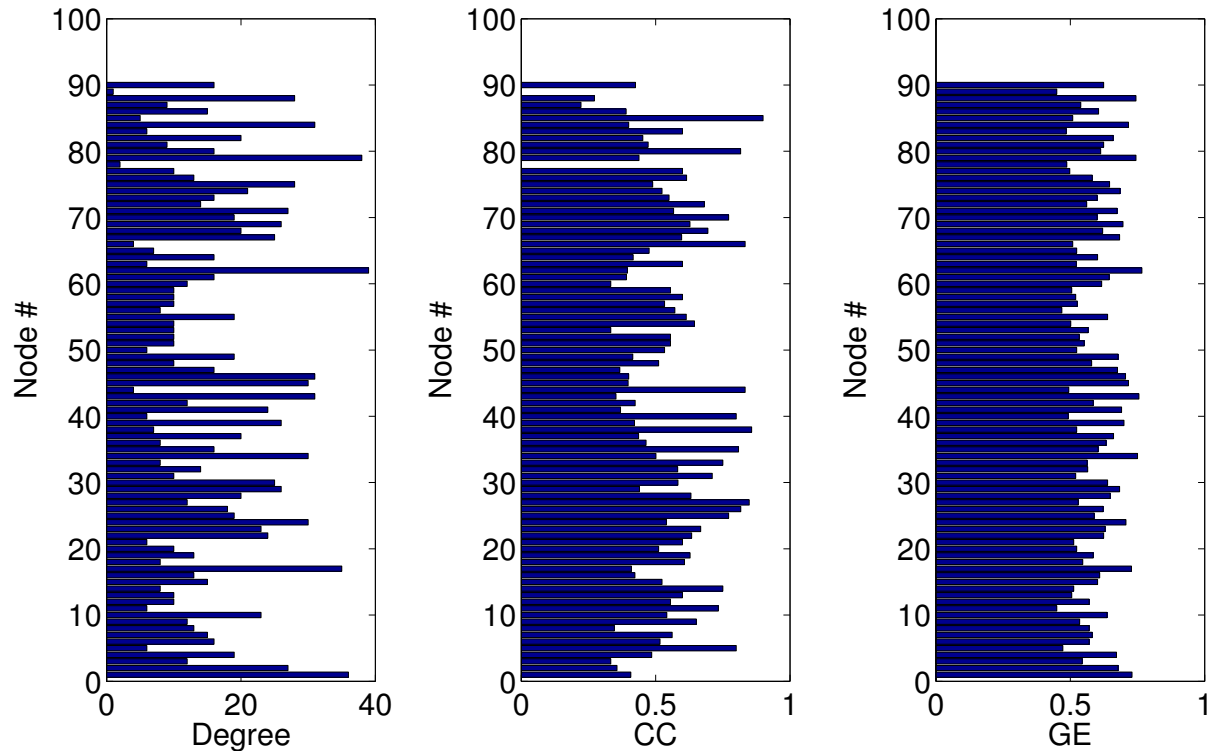


FIG. 9. **Node-wise complex network measures of the human brain functional interactions.** Degree, clustering coefficient (CC) and global efficiency (GE) of the network nodes of the empirical functional connectivity used in the simulations as coupling topology (threshold $r = 0.57$).

V. CONCLUSION

A main conclusion of our work is that fast flexible changes in neural network synchrony contribute to the emergence of correlated BOLD activity. By tuning the brain network topology and the dynamical interactions between the regions (network nodes), we show that the model agreement with the experiment is the best for a dynamical state that maximizes synchrony and variations in synchrony. These results support our hypothesis that highly variable, metastable network dynamics may facilitate transitions between network configurations.

VI. ACKNOWLEDGMENTS

This work was supported by BMBF (grant no. 01Q1001B) in the framework of BCCN Berlin (Project B7). We thank John-Dylan Haynes and his group for helpful discussions concerning the fMRI data analysis and Yasser Iturria-Medina for sharing the DTI data used in the study.

¹Bassett, D. S., Wymbs, N. F., Porter, M. A., Mucha, P. J., Grafton, S. T., 2014. Cross-linked structure of network evolu-

tion. *Chaos: An Interdisciplinary Journal of Nonlinear Science* 24 (1), 013112.

²Biswal, B., Yetkin, F. Z., Haughton, V. M., Hyde, J. S., 1995. Functional connectivity in the motor cortex of resting human brain using echo-planar mri. *Magnetic Resonance in Medicine* 34 (4), 537–541.

³Bogacki, P., Shampine, L. F., 1989. A 3(2) pair of runge - kutta formulas. *Applied Mathematics Letters* 2 (4), 321–325.

⁴Breakspear, M., Heitmann, S., Daffertshofer, A., 2010. Generative models of cortical oscillations: neurobiological implications of the Kuramoto model. *Frontiers in human neuroscience* 4.

⁵Bullmore, E. T., Sporns, O., 2009. Complex brain networks: graph theoretical analysis of structural and functional systems. *Nat. Rev. Neurosci.* 10 (3), 186–198.

⁶Bullmore, E. T., Sporns, O., 2012. The economy of brain network organization. *Nature Reviews Neuroscience* 13 (5), 336–349.

⁷Cabral, J., Fernandes, H. M., Van Hartevelt, T. J., James, A. C., Kringelbach, M. L. e. a., 2013. Structural connectivity in schizophrenia and its impact on the dynamics of spontaneous functional networks. *Chaos: An Interdisciplinary Journal of Nonlinear Science* 23 (4), 046111.

⁸Cabral, J., Hugues, E., Kringelbach, M. L., Deco, G., 2012. Modeling the outcome of structural disconnection on resting-state functional connectivity. *NeuroImage* 62, 1342–1353.

⁹Cabral, J., Hugues, E., Sporns, O., Deco, G., 2011. Role of local network oscillations in resting-state functional connectivity. *NeuroImage* 57 (1), 130–139.

¹⁰Damoiseaux, J. S., Rombouts, S. A. R. B., Barkhof, F., Scheltens, P., Stam, C. J., Smith, S. M., Beckmann, C. F., 2006. Consistent resting-state networks across healthy subjects. *Proc. Natl. Acad.*

- Sci. U.S.A. 103 (37), 13848–13853.
- ¹¹Deco, G., Jirsa, V. K., 2012. Ongoing cortical activity at rest: criticality, multistability, and ghost attractors. *The Journal of Neuroscience* 32 (10), 3366–3375.
 - ¹²Deco, G., Jirsa, V. K., McIntosh, A. R., 2011. Emerging concepts for the dynamical organization of resting-state activity in the brain. *Nature Reviews Neuroscience* 12 (1), 43–56.
 - ¹³Deco, G., Jirsa, V. K., McIntosh, A. R., Sporns, O., Kötter, R., 2009. Key role of coupling, delay, and noise in resting brain fluctuations. *Proc. Natl. Acad. Sci. U.S.A.* 106 (25), 10302–10307.
 - ¹⁴Deco, G., Senden, M., Jirsa, V. K., 2012. How anatomy shapes dynamics: a semi-analytical study of the brain at rest by a simple spin model. *Frontiers in computational neuroscience* 6.
 - ¹⁵Flunkert, V., Schöll, E., 2009. pydelay – a python tool for solving delay differential equations. arXiv:0911.1633 [nlin.CD].
 - ¹⁶Friston, K., Holmes, A. P., Worsley, K. J., Poline, J.-P., Frith, C. D., Frackowiak, R., 1994. Statistical parametric maps in functional imaging: a general linear approach. *Human brain mapping* 2 (4), 189–210.
 - ¹⁷Friston, K., Mechelli, A., Turner, R., Price, C. J., 2000. Nonlinear responses in fMRI: The balloon model, Volterra kernels, and other hemodynamics. *NeuroImage* 12 (4), 466–477.
 - ¹⁸Ghosh, A., Rho, Y., McIntosh, A. R., Kötter, R., Jirsa, V. K., 2008. Cortical network dynamics with time delays reveals functional connectivity in the resting brain. *Cogn. Neurodyn.* 2 (2), 115–120.
 - ¹⁹Ghosh, A., Rho, Y., McIntosh, A. R., Kötter, R., Jirsa, V. K., 2008. Noise during rest enables the exploration of the brain’s dynamic repertoire. *PLoS Comput Biol* 4 (10), e1000196.
 - ²⁰Hellyer, P. J., Shanahan, M., Scott, G., Wise, R. J. S., Sharp, D. J., Leech, R., 2014. The control of global brain dynamics: Opposing actions of frontoparietal control and default mode networks on attention. *J. Neuroscience* 34 (2), 451–461.
 - ²¹Honey, C. J., Kötter, R., Breakspear, M., Sporns, O., 2007. Network structure of cerebral cortex shapes functional connectivity on multiple time scales. *Proc. Natl. Acad. Sci. U.S.A.* 104, 10240–10245.
 - ²²Honey, C. J., Sporns, O., Cammoun, L., Gigandet, X., Thiran, J. P., Meuli, R., Hagmann, P., 2009. Predicting human resting-state functional connectivity from structural connectivity. *Proceedings of the National Academy of Sciences of the United States of America* 106 (6), 2035–2040.
 - ²³Iturria-Medina, Y., Sotero, R. C., Canales-Rodríguez, E. J., Alemán-Gómez, Y., Melie-García, L., 2008. Studying the human brain anatomical network via diffusion-weighted mri and graph theory. *Neuroimage* 40 (3), 1064–1076.
 - ²⁴Izhikevich, E. M., Kuramoto, Y., 2006. Weakly coupled oscillators. *Encyclopedia of mathematical physics* 5, 448.
 - ²⁵Margulies, D. S., Kelly, A. M. C., Uddin, L. Q., Biswal, B. B., Castellanos, F. X., Milham, M. P., 2007. Mapping the functional connectivity of anterior cingulate cortex. *NeuroImage* 37 (2), 579–588.
 - ²⁶Newman, M. E. J., 2010. *Networks: an introduction*. Oxford University Press, Inc., New York.
 - ²⁷Nguyen, L. H., Hong, K.-S., 2011. Synchronization of coupled chaotic fitzhugh–nagumo neurons via lyapunov functions. *Mathematics and Computers in Simulation* 82 (4), 590–603.
 - ²⁸Nicosia, V., Valencia, M., Chavez, M., Díaz-Guilera, A., Latora, V., 2013. Remote synchronization reveals network symmetries and functional modules. *Phys. Rev. Lett.* 110, 174102.
 - ²⁹Omelchenko, I., Omel’chenko, O. E., Hövel, P., Schöll, E., 2013. When nonlocal coupling between oscillators becomes stronger: patched synchrony or multichimera states. *Phys. Rev. Lett.* 110, 224101.
 - ³⁰Panchuk, A., Rosin, D. P., Hövel, P., Schöll, E., 2013. Synchronization of coupled neural oscillators with heterogeneous delays. *Int. J. Bifurcation Chaos* 23 (12), 1330039.
 - ³¹Pikovsky, A., Rosenblum, M. G., Kurths, J., 2001. *Synchronization, A Universal Concept in Nonlinear Sciences*. Cambridge University Press, Cambridge.
 - ³²Roy, D., Sigala, R., Breakspear, M., McIntosh, A. R., Jirsa, V. K., 2014. Using the virtual brain to reveal the role of oscillations and plasticity in shaping brain’s dynamical landscape. *Brain Connectivity*.
 - ³³Rubinov, M., Sporns, O., 2010. Complex network measures of brain connectivity: uses and interpretations. *NeuroImage* 52 (3), 1059–1069.
 - ³⁴Seth, A. K., Chorley, P., Barnett, L. C., 2013. Granger causality analysis of fmri bold signals is invariant to hemodynamic convolution but not downsampling. *Neuroimage* 65, 540–555.
 - ³⁵Shampine, L. F., Thompson, S., 2001. Solving DDEs in Matlab. *Appl. Num. Math.* 37 (4), 441–458.
 - ³⁶Shanahan, M., 2010. Metastable chimera states in community-structured oscillator networks. *Chaos: An Interdisciplinary Journal of Nonlinear Science* 20 (1), 013108.
 - ³⁷Strogatz, S. H., 2000. From Kuramoto to Crawford: exploring the onset of synchronization in populations of coupled oscillators. *Physica D* 143, 1–20.
 - ³⁸Tzourio-Mazoyer, N., Landeau, B., Papathanassiou, D., Crivello, F., Etard, O., Delcroix, N., Mazoyer, B., Joliot, M., 2002. Automated anatomical labeling of activations in SPM using a macroscopic anatomical parcellation of the MNI MRI single-subject brain. *Neuroimage* 15 (1), 273–289.
 - ³⁹van Wijk, B. C., Stam, C. J., Daffertshofer, A., 2010. Comparing brain networks of different size and connectivity density using graph theory. *PLoS One* 5 (10), e13701.
 - ⁴⁰Vincent, J. L., Patel, G. H., Fox, M. D., Snyder, A. Z., Baker, J. T., Van Essen, D. C., Zempel, J. M., Snyder, L. H., Corbetta, M., Raichle, M. E., 2007. Intrinsic functional architecture in the anesthetized monkey brain. *Nature* 447 (7140), 83–86.
 - ⁴¹Vuksanović, V., Hövel, P., 2014. Functional connectivity of distant cortical regions: Role of remote synchronization and symmetry in interactions. *NeuroImage* 97, 1–8.

TABLE I. Cortical and sub-cortical regions as defined in the automated anatomic labelling (AAL) template image.

Index	Anatomical Description	Label
1	Precentral	PRE
2	Frontal Sup	F1
3	Frontal Sup Orb	F10
4	Frontal Mid	F2
5	Frontal Mid Orb	F20
6	Frontal Inf Oper	F30P
7	Frontal Inf Tri	F3T
8	Frontal Inf Orb	F30
9	Rolandic Oper	RO
10	Supp Motor Area	SMA
11	Olfactory	OC
12	Frontal Sup Medial	F1M
13	Frontal Mid Orb	SMG
14	Gyrus Rectus	GR
15	Insula	IN
16	Cingulum Ant	ACIN
17	Cingulum Mid	MCIN
18	Cingulum Post	PCIN
19	Hippocampus	HIP
20	ParaHippocampal	PHIP
21	Amygdala	AMYG
22	Calcarine	V1
23	Cuneus	Q
24	Lingual	LING
25	Occipital Sup	O1
26	Occipital Mid	O2
27	Occipital Inf	O3
28	Fusiform	FUSI
29	Postcentral	POST
30	Parietal Sup	P1
31	Parietal Inf	P2
32	Supra Marginal Gyrus	SMG
33	Angular	AG
34	Precuneus	PQ
35	Paracentral Lobule	PCL
36	Caudate	CAM
37	Putamen	PUT
38	Pallidum	PAL
39	Thalamus	THA
40	Heschi	HES
41	Temporal Sup	T1
42	Temporal Pole sup	T1P
43	Temporal Mid	T2
44	Temporal Pole Mid	T2P
45	Temporal Inf	T3

Indexes from 1-45 indicate order in which regions in the right hemisphere are arranged in all connectivity/adjacency matrices presented throughout the paper. For the respective regions in the left hemisphere, the index needs to be shifted by 45.